JACS
JOURNAL OF THE AMERICAN CHEMICAL SOCIETY

ARTICLE

pubs.acs.org/JACS

Fluorinating Hexagonal Boron Nitride into Diamond-Like Nanofilms with Tunable Band Gap and Ferromagnetism

Zhuhua Zhang,[†] Xiao Cheng Zeng,[*,‡] and Wanlin Guo[*,†]

[†]Institute of Nano Science and Key Laboratory of Intelligent Nano Materials and Devices of Ministry of Education, Nanjing University of Aeronautics and Astronautics, Nanjing 210016, China

[‡]Department of Chemistry and Center for Materials & Nanoscience, University of Nebraska—Lincoln, Lincoln, Nebraska 68588, United States

Supporting Information

ABSTRACT: Cubic boron nitride (*c*-BN) possesses a number of extreme properties rivaling or surpassing those of diamond. Especially, owing to the high chemical stability, *c*-BN is desired for fabricating electronic devices that can stand up to harsh environments. However, realization of *c*-BN-based functional devices is still a challenging task due largely to the subtlety in the preparation of high-quality *c*-BN films with uniform thickness and controllable properties. Here, we present a simple synthetic strategy by surface fluorination of few-layered hexagonal boron nitride (*h*-BN) sheets to produce thermodynamically favorable F-terminated *c*-BN nanofilms with an embedded N−N bond layer and strong inbuilt electric polarization. Due to these specific features, the fluorinated *c*-BN nanofilms have controllable band gap by thickness or inbuilt and applied electric fields. Especially, the produced nanofilms can be tuned into substantial ferromagnetism through electron doping within a reasonable level. The electron-doping-induced deformation ratio of the *c*-BN nanofilms is found to be 1 order of magnitude higher than those of carbon nanotubes and graphene. At sufficient high doping levels, the nanofilm can be cleaved peculiarly along the N−N bond layer into diamond-like BN films. As the proposed synthesis strategy of the fluorinated *c*-BN nanofilms is well within the reach of current technologies, our results represent an extremely cost-effective approach for producing high-quality *c*-BN nanofilms with tunable electronic, magnetic, and electro-mechanical properties for versatile applications.

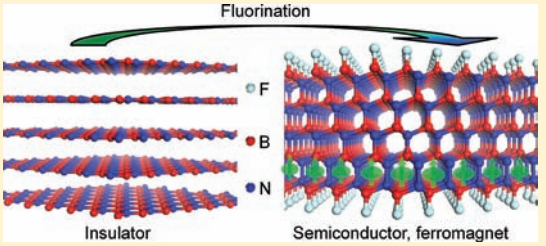

1. INTRODUCTION

Cubic boron nitride (*c*-BN) has the same sp^3 bond structure as diamond and hence possesses outstanding mechanical, thermal, and optical properties second only to diamond.[1−3] In particular, the ionicity of B−N bonds entails *c*-BN a wider band gap, greater chemical inertness, and higher oxidation stability over other diamond-like materials.[4] This unique combination of properties in *c*-BN provides many special prospects in applications, such as high-power and high-temperature devices operating in extreme environments. However, *c*-BN's merits have not been fully exploited in practice because of severe limitations in its synthesis and electronic properties. First, the preparation of high-quality *c*-BN presents a significant challenge, even more difficult than the synthesis of diamond due to the very different electronegativity of boron and nitrogen.[4] Most of the previously fabricated nanofilms,[5] either by physical[6] or by chemical vapor deposition[7−10] techniques, are usually in polycrystalline form and adhered by amorphous or turbostratic BN around crystal domains.[8,11] Yet for practical applications, it is optimal to have *c*-BN nanofilms with uniform crystallization and designable thickness. Second, *c*-BN is intrinsically an insulator with wide energy gap over 6 eV, which is far beyond the gap values (<3 eV) desired for most of the current electronic and optical devices.[12] To be widely used in functional devices, semiconducting forms of *c*-BN with versatile properties are necessary but have never been reported.

Recent experimental studies have shown that by heating the mixture of graphene sheets and XeF_2 fluorination of a suspended graphene monolayer can be achieved, and in the final product of fluorographene each carbon atom is covalently attached with a fluorine atom.[13,14] We expect that by using a similar experimental strategy one should be able to transform the hexagonal boron nitride (*h*-BN) sheet into a fluorinated sp^3-bonded BN film whose structure will be equivalent to that of a monolayer *c*-BN(111) film.[15] This strategy is particularly viable for the *h*-BN layer because it has been known that chemisorption of fluorine atoms on BN nanostructures exhibits strong site preference to uniformly bond with boron atoms (determined by the large difference in their electronegativity),[16−18] whereas on single-side graphene fluorine atoms tend to form disordered clusters.[19,20] This selective chemisorption may become more crucial in fluorinating *h*-BN multilayers, as it opens a possibility to form high-quality *c*-BN nanofilms. Nevertheless, the ground-state

Received: July 19, 2011
Published: August 11, 2011

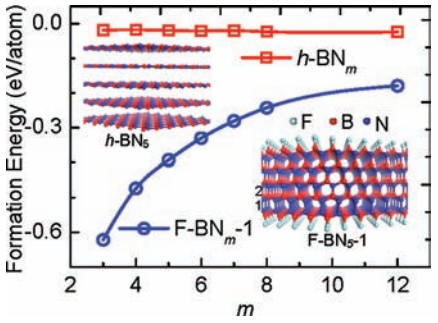

Figure 1. Structure and energetics in h-BN_m sheets and fluorinated F-BN_m nanofilms. Formation energies of the h-BN_m sheets and the F-BN_m-1 nanofilms as functions of m. Insets are the front views of atomic structures for (top) the h-BN_5 sheet and (bottom) the F-BN_5-n nanofilm, with n = 1 here.

structure and properties of the fluorinated h-BN multilayers remain largely unknown, even though the h-BN multilayers have been produced in previous experiments.[21]

In this article, we show by comprehensive first-principles calculations that fluorinating few-layered h-BN sheets can trigger a spontaneous formation of c-BN nanofilms of the ground state. The nanofilm contains a unique homogeneous N−N bond layer and changes quickly from wide-gap semiconductor to quasi-metal with increasing film thickness. More interestingly, by electron doping, the nanofilms show a novel ferromagnetic spin state and an exceptionally large deformation and even suffer a cleavage along the N−N bond layer to form two thinner c-BN films. These unique features render such nanofilms very promising for broad applications in nanoelectronics, photovoltaics, and actuators.

2. THEORY AND METHODS

All the calculations are performed by using the Vienna Ab-initio Simulation Package (VASP).[22,23] The projector-augmented wave method[24] for the core region and the local density approximation (LDA) for the exchange correlation potential are employed. It is known that semilocal generalized gradient approximation (GGA) largely overestimates the interlayer distance in graphite or h-BN sheets, while the LDA can give reasonable interlayer distances in these systems. So we employ LDA for the exchange correlation potential. We confirm that both the LDA and GGA (with PBE function) agree well with each other in the calculated electronic properties. A kinetic energy cutoff of 500 eV is chosen in the plane-wave expansion. We use an initial lattice constant of 1.44 Å and a 2 × 2 h-BN supercell to perform structural optimization. A vacuum region of 15 Å is set between two adjacent images. In the few-layered h-BN with AB stacking among the layers, we let the B atom of one layer directly above an N atom of the adjacent layer and let the N atom centered above a BN hexagon in the adjacent layer. The two-dimensional Brillouin zone integration is sampled by 60 special k-points. Both the atomic positions and supercell shape are allowed to relax until the force on each atom is less than 0.01 eV/Å. The external electric field is introduced by the planar dipole layer method.[25]

3. RESULTS AND DISCUSSION

For ease of discussion, we denote the m-layered h-BN as h-BN_m and the corresponding F-terminated sp^3-bonded h-BN_m nanofilm as F-BN_m. When the h-BN_m sheet is fluorinated in a similar manner for synthesizing fluorographene,[13,14] both outmost surfaces of the F-BN_m nanofilm will be terminated by fluorinated B atoms due to the aforementioned preference of chemisorptions. This will produce a layer of homogeneous N−N bonds in the nanofilm as shown by the bottom inset of Figure 1. We confirm that such an F-BN_m nanofilm is the most stable configuration among all other possible polymorphs (see Supporting Information for detailed comparison). Since the N−N bond layer can arise at different positions in the multilayered nanofilm, we denote the F-BN_m nanofilm with the N−N bond layer at position n as F-BN_m-n (see the marked 1 and 2 in the bottom inset of Figure 1 for the F-BN_5 nanofilm). Generally, the F-BN_m-1 is energetically the most favorable among various values of n in the F-BN_m-n, and the energetic preference becomes more distinguished in a thicker nanofilm with the N−N bond layer being more favorable as the subsurface layer.

Before introducing the transformation, we calculate the formation energy to compare the relative stability of the h-BN_m sheet and F-BN_m film, and it is defined as

$$E_f = E_{coh} - N_B\mu_B - N_N\mu_N - N_F\mu_F \quad (1)$$

where E_{coh} is the cohesive energy per atom in the sheet or nanofilms; N_i (i = B,N, F) is the number of i atoms in the supercell; and μ_i is the corresponding chemical potential. As the precursor materials consist wholly of BN sheets, we choose $\mu_B + \mu_N$ as the cohesive energy per BN pair of a h-BN sheet and μ_F as the cohesive energy per atom in a F molecule. Figure 1 demonstrates that the formation energy of the F-BN_m nanofilm increases rapidly with increasing thickness, while that of the h-BN_m sheet decreases smoothly. Within our calculated range of m, the F-BN_m nanofilm has significantly lower formation energy than the corresponding h-BN_m sheet, particularly in the case of thinner nanofilms. The above results strongly indicate that the F-BN_m nanofilm is remarkably more stable than the h-BN_m, especially for smaller m. Note that the LDA results do not consider the correction of van der Waals interaction energy, but the correction only reduces the formation energy of the h-BN_m sheet by 0.03−0.04 eV/atom.[26] So our results remain essentially unchanged upon this correction. The higher stability of the nanofilm over the h-BN_m sheet is because of the increased ratio of surface atoms which contributes a low surface energy upon fluorine termination in light of that the binding energy of the F−B bond (4.15 eV) is distinctly larger than the F−F bond (2.08 eV). The remarkably high stability of the BN nanofilm is unique to the F-termination and does not exist for other chemical terminations. For example, correspondingly H-terminated nanofilms are less stable than multilayered h-BN sheets. In brief, this energetics comparison strongly implicates an explicit route of fluorinating a few-layered h-BN sheet into an sp^3-bonded BN nanofilm.

In what follows, we investigate the transformation process of the h-BN_m upon fluorination. Indeed, the fluorinated h-BN_5 sheet can spontaneously transform into an F-BN_5 nanofilm during the structural relaxation (see Supporting Information, Movie 1). The energy profile for the transition from the fluorinated h-BN_5 sheet to the F-BN_5 nanofilm is shown in Figure 2a, together with the atomic structures of four chosen images A, B, C, and D along the energy profile. In image A, the two outermost BN layers exhibit zigzag buckling upon chemisorption of F atoms on B atoms. Meanwhile, active dangling bond states are created and distributed on N atoms, rendering

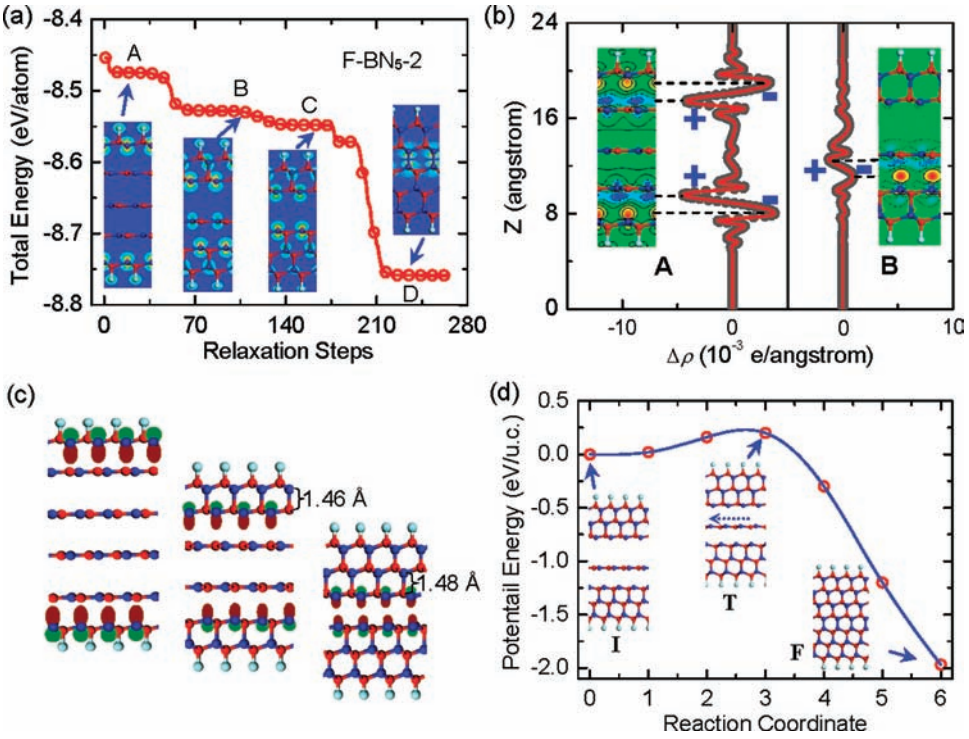

Figure 2. Formation of F-BN_5-2 nanofilm from the *h*-BN_5 sheet and the driving mechanism. (a) Total energy variation during the structural relaxation for the fluorinated *h*-BN_5. Inset: four images A, B, C, and D in the relaxation pathway, with the electronic states around the Fermi level plotted in these images. (b) Plane-averaged difference in electron densities, $\Delta\rho_A = \rho_A(z) - \rho_{15}(z) - \rho_{234}(z)$ amd $\Delta\rho_B = \rho_B(z) - \rho_{123}(z) - \rho_{45}(z)$, showing the interlayer charge displacement in the images A and B, where $\rho_{xy}(z)$ is the plane-averaged charge density of the *x*th plus *y*th BN layers along the *z* direction. Insets show their corresponding isosurface plots of the charge displacement. The horizontal dashed lines mark the positions of the charge depletion and accumulation regions, between which the distances are identical in images A and B. (c) Schematic map for the decayed reactivity of the radicals during the transformation from the fluorinated *h*-BN_6 sheet toward the F-BN_6 nanofilm. The different reactivity is illustrated by the sizes of charge density isosurfaces. (d) Calculated minimum-energy path for the transition from the fluorinated *h*-BN_7 sheet to the F-BN_7 nanofilm. Insets show the atomic structures of initial (I), transition (T), and final (F) states along this energy path.

the N atoms to become radical sites. In image B, the interlayer bonds are formed between both the two higher *h*-BN layers and the two lower BN layers, with only the third BN layer being isolated, followed by a downshift of energy step. As the relaxation continues, the third layer preferentially forms interlayer bonds with the fourth layer due to the better stacking between them (see image C), and then the N radicals on the second and third *h*-BN layers disappear upon formation of homogeneous N—N bonds. This results in a considerable energy gain and announces the formation of an F-BN_5-2 nanofilm shown in image D. This process is reproduced in our ab initio molecular dynamics simulations at 200 K, and the formed F-BN_m nanofilms can be structurally very stable up to 2000 K as confirmed by our subsequent 5 ps simulation (see Figure S3 in Supporting Information). This transformation also occurs in other interlayer stacking modes (such as the ABC stacking) and even enables the formation of hybrid *c*-BN/diamond nanofilms when inserting graphene layers into the *h*-BN_m. Experimentally, we expect that the synthesis of *c*-BN nanofilms can be realized by heating the mixture of *h*-BN sheets and XeF_2, as done for synthesizing fluorographene.[13,14]

To explore the mechanism underlying the spontaneous interlayer bond formation, we plot the plane-averaged charge redistribution along the normal of the image A, as shown in Figure 2b. We observe significant electron transfer from the second to the first BN layer as well as from the fourth layer to the fifth layer, giving rise to electric dipoles between these layers. This is attributed to the active N radicals in the two outermost BN layers which have high potential for accepting electrons, similar to unbonded F atoms. The formation of interlayer bonds is highly favorable with the charge transfer, as it not only enhances the interlayer interaction by imposing a Coulomb attraction between these adjacent layers but also attenuates the B—N bonds in the second and fourth layers so that they can be flexibly buckled to achieve sp^3 hybridization. The charge transfer becomes more favorable with decreasing interlayer separation and thus rapidly promotes the bond formation. Similar charge transfer is also found between the third and fourth BN layers in image B, at the same interlayer distance as that between the second and first BN layers in image A. This layer-by-layer charge transfer provokes a layer-by-layer buckling in the fluorinated *h*-BN_5 sheet. One should note that the charge transfer in image B is less pronounced, indicating that the activity of the N radicals is degraded in the fourth layer, as evidenced by the more extended distribution of dangling bond charge density in the image B than in the image A (Figure 2b). This is understandable by examining their atomic structures: the buckling in the first BN layer in image A is 0.38 Å, and the N atoms show more sp^3 character; whereas the buckling in the second layer of image B is only 0.27 Å due to the strained bonding from the first layer, thus keeping more sp^2 character with less dangling bond states in this layer. The buckling in the frontier BN layer is further reduced when the

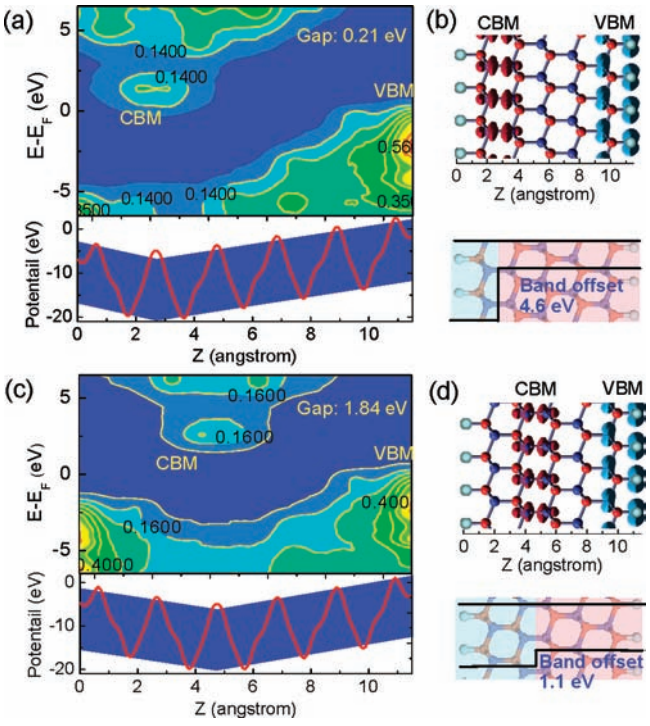

Figure 3. Electronic structures of the F-BN_5-*n* nanofilms. (a) Spatially resolved local density of states (top) and plane-averaged electrostatic potential (bottom) along the normal (*z*-direction) of the F-BN_5-1 nanofilm. The blue shades guide the trend of potential variation across the nanofilm. (b) Top: Isosurface plot (0.2 e/Å^3) of partial charge densities for the VBM and CBM of the F-BN_5-1 nanofilm. Bottom: Schematic illustration of the band alignment in the nanofilm. (c−d) Corresponding cases for the F-BN_5-2 nanofilm are present in (c) and (d), respectively.

interlayer bonds continue to form in the *h*-BN_m sheet, making the N radials increasingly inactive (see Figure 2c). Consequently, spontaneous formation of the F-BN_m nanofilm upon fluorination can be achieved only when $m < 7$. For $m \geq 7$, fully relaxing the fluorinated *h*-BN_7 sheet results in a mixed multilayered structure of *c*-BN and *h*-BN (see inset I in Figure 2d). However, this mixed structure is energetically less favorable than the F-BN_7 nanofilm by 1.97 eV per unit cell. So the full transformation of an F-BN_7 nanofilm should be stopped by an energy barrier. Using the nudged elastic band method,[27] we calculate the minimum energy path and determine an energy barrier of about 0.2 eV within the path (Figure 2d), mainly due to the energy cost to parallel move the middle *h*-BN layer and buckle it for interlayer bond formation (see inset T in Figure 2d). This energy barrier increases with increasing *m* and eventually renders the synthesis strategy unfeasible.

If the F-BN_m nanofilms are synthesized, one should be curious whether the nanofilms possess novel electronic properties and their thickness dependence. To this end, we show the spatially resolved local density of states (LDOS) along the normal of the F-BN_5-1 and F-BN_5-2 nanofilms in Figures 3a and 3c, respectively. Surprisingly, the F-BN_5-1 and F-BN_5-2 films are predicted to have energy gaps of only 0.21 and 1.84 eV, respectively, sharply reduced from 4.0 eV in bulk *h*-BN and 4.4 eV in bulk *c*-BN (from the LDA calculations). We also perform GW calculations which estimate the band gaps being around 1.5 and 3.2 eV for the F-BN_5-1 and F-BN_5-2 films, respectively, still significantly reduced from the experimental values of 5.8 eV for the *h*-BN sheets and 6.2 eV for the bulk *c*-BN. Wave function analysis shows that the conduction band minimum (CBM) stems from the p_z orbitals of the atoms forming the N−N bond layer, whereas the valence band maximum (VBM) stems from the p_y orbitals of the terminated F atoms on the lower film surface and subsurface N atoms nearby, which are further away from N−N bond layer than the other surface (see Figures 3b and 3d). The naturally well-separated distribution of hole and electron states is ideally suited for photovoltaic applications.[28] Structurally speaking, one could view that the nanofilm is composed of two single-crystal *c*-BN slabs head-to-head bonded together at the N side or a natural heterostructure. It is interesting that the band offset in such a heterostructure can be strongly tunable by varying the location of the N−N bond layer, from 4.6 eV in the F-BN_5-1 nanofilm to 1.1 eV in the F-BN_5-2 film (see Figures 3b and d). This result indicates that the degree of carrier (hole) confinement in the nanofilms strongly depends on the localization of the N−N bond layer.

To elucidate the origin of the reduced energy gap, we plot the plane-averaged electrostatic potentials along the normal of the two nanofilms, as shown in the bottoms of Figures 3a and 3c. Interestingly, the electrostatic potential shows a minimum at the N−N bond layer and a maximum at the film surface where the VBM is located, quite akin to the energy change of the spatially resolved near-gap states across the film thickness. Clearly, a local build-in electric potential difference is generated in the nanofilms due to different site potentials of N and B atoms. The averaged potential differences between the VBM and CBM planes, $P_{VBM}-P_{CBM}$, are 7.49 and 5.98 eV in the F-BN_5-1 and F-BN_5-2 nanofilms, respectively. With this potential difference, the energy level of the CBM is shifted downward, while that of the VBM is shifted upward, leading to a decrease in the energy gap of the nanofilms. Note that the presence of the N−N bond layer retards the gap reduction in the film, especially when it is around the middle of the film. As the gap reduction is very similar to the Stark effect in semiconductors or insulators subject to an external electric field, we use the *inherent Stark effect* to describe it. In fact, a similar *inherent Stark effect* induced by the build-in electric polarization is also present in zigzag BN nanoribbons.[25,26] However, the *inherent Stark effect* demonstrated here is considerably more pronounced than that in the sp^2-bonded BN nanoribbons. This is mainly due to their different orientation of the near-gap orbitals. In the sp^3-bonded nanofilms, the CBM has a nodal plane vertical to the build-in electric field, which enables a strong charge redistribution upon the inherent potential difference, in contrast to the case in sp^2 nanoribbons whose CBM (π^*) has a nodal plane parallel to the build-in electric field.

In view of the strong dependence of band gap on the build-in potential difference, it is important to investigate the thickness effect on the energy gaps of the nanofilms (LDA calculation). Figure 4a shows that the LDA gap decreases monotonically from 3.84 eV in the F-BN_3-1 nanofilm to zero in the F-BN_7-1 film. The same trend of gap variation also appears in the film groups of F-BN_m-2 and -3. In particular, all the gaps of the F-BN_m-1 films are direct and formed at the Brillouin center, while all the gaps of F-BN_m-2 and 3 films are indirect because the CBM in the F-BN_m-1 films behaves more like a surface state (Figure 3b). To understand the thickness dependence for the energy gap, we plot $P_{VBM}-P_{CBM}$ for the nanofilms as a function of the thickness in Figure 4a. We find that $P_{VBM}-P_{CBM}$ is typically higher in a

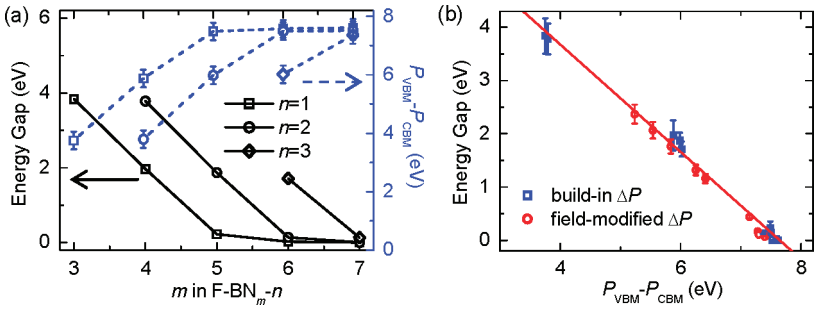

Figure 4. Energy gap of the F-BN$_m$-n nanofilm. (a) Energy gap as a function of the thickness m (solid curves) and the thickness dependence of the potential difference (dash curves), $P_{VBM}-P_{CBM}$, between the two planes where VBM and CBM are, respectively, concentrated. (b) Energy gap vs the build-in and electric-field-modified $P_{VBM}-P_{CBM}$.

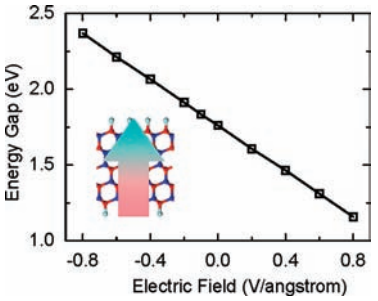

Figure 5. Electric-field-induced modulation on the energy gap of the F-BN$_5$-2 nanofilm. The electric field is applied along the normal of the nanofilm as shown in the inset, with the positive direction being indicated by the big arrow.

thicker nanofilm that has a smaller gap. With varying the position of the N−N bond layer, the $P_{VBM}-P_{CBM}$ is still exactly proportional to the energy gap. This clearly demonstrates that the increased build-in potential difference is the major origin of the reduced gap in thicker F-BN$_m$-n nanofilms, whereas the weakened quantum confinement and surface effects play trivial roles in the gap reduction (not shown). To be clearer, we plot the energy gap of all nanofilms as a function of $P_{VBM}-P_{CBM}$ in Figure 4b. It is obvious that a roughly linear relationship is in place between the energy gap and $P_{VBM}-P_{CBM}$.

The above results have established that the build-in potential difference determines the energy gap of the F-BN$_m$ nanofilms by Stark effect. We consider applying a vertical electric field to the nanofilm to tune the potential difference, which should result in tunable gap in the F-BN$_m$ nanofilms. Here, we define the electric field pointing from the VBM site to the CBM site as the positive field. The response of the energy gap in the F-BN$_5$-2 nanofilm to the applied electric field is shown in Figure 5. The energy gap is reduced linearly with the positive field but increased with negative field, just because a positive field enhances the build-in potential difference while a negative field reduces it. Note that this field-induced gap modulation is entirely from the Stark effect as evidenced by the nearly linear relationship and does not refer to nearly free electron bands as demonstrated in BN nanotubes and nanoribbons.[29,30] In Figure 4b, we also present the energy gap as a function of the modified $P_{VBM}-P_{CBM}$ in the case of applying a vertical external electric field. It is interesting that the function falls in the same line as that of energy gap versus build-in potential difference. Similar energy gap modulation by the electric field also holds for other F-BN$_m$ films, with tunable magnitude determined by the coupled effect of film thickness and their energy gaps. The tunable band gap via the control of the thickness and external electric field entails great flexibility in design and optimization of BN-based devices.

While the semiconducting properties are robust in the synthesized F-BN$_m$ nanofilms, it is still important to examine their response to carrier doping because most devices proposed for the nanofilms rely on their carrier transport performance. In particular, the F-BN$_m$ nanofilm contains a layer of N−N bonds, which should embody much richer chemical behavior upon carrier doping as nitrogen has high Pauli electronegativity. Here, we mainly focus on the electron doping since the N−N bond layer is just where the CBM distributes. Surprisingly, once extra electrons are doped, both the F-BN$_5$-1 and F-BN$_5$-2 nanofilms exhibit substantial magnetism. Figure 6a shows that the magnetic moment arises in the F-BN$_5$-2 nanofilm if extra electrons are over 0.1 e per supercell, and the polarized electron spins are mostly contributed by the atoms in the N−N bond layer (see inset in Figure 6a). The net magnetic moment is generally larger at higher doping levels and can reach up to 0.36 μ_B at a level of 0.4 e extra electrons, of which about 0.3 μ_B is from the 2p$_z$ orbital of the two mutually bonded N atoms. As such, the magnetic moment does not significantly depend on nanofilm thickness. We then double the supercell size and compare the energies of different magnetic orderings to determine the magnetic coupling between local spins. It is desirable that the ferromagnetic state appears to be always the ground state. Under a doping level of 0.3 electrons, the ferromagnetic state becomes more stable than the antiferromagnetic state by 6 meV/supercell and 20 meV more stable than the nonmagnetic state. These two energetic differences increase rapidly with increasing doping level. Similar magnetic behavior is also revealed in the F-BN$_5$-1 nanofilm, but the magnetism starts to emerge at a higher doping level of 0.4 e/supercell owing to the stronger delocalization of the near-gap states. Here, the magnetism in the BN nanofilms can be confirmed through GGA calculations as well, which even yield stronger magnetism as shown by the dashed lines in Figure 6a, especially in the case of the F-BN$_5$-1 nanofilm.

The origin of the ferromagnetism in the nanofilms can be understood from the response of the N−N bonds to the electron doping. As shown in Figure 3b, the CBM of the nanofilm exhibits a feature of antibonding state distributing around the N−N bonds. Extra electrons will then drop into the CBM state and hence reside around the N−N bond, which will greatly enhance the Pauli repulsion between the two N atoms, thereby stretching the N−N bonds. The weakened N−N bonds localize the CBM

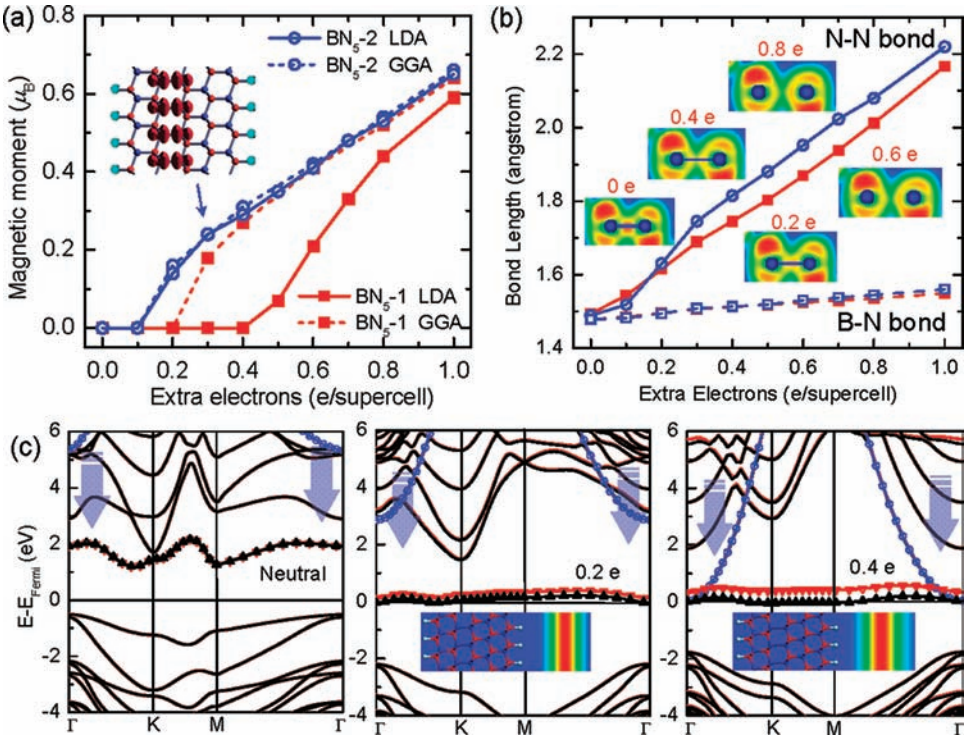

Figure 6. Electron doping induced magnetism and bond deformation in the F-BN_5 nanofilms. (a) Net magnetic moment calculated with LDA and GGA as functions of doped electrons per unit cell in the F-BN_5-1 and F-BN_5-2 nanofilms. Insets show isosurface plots (0.02 e/Å^3) of the magnetization density when the F-BN_5-2 nanofilm is under a doping level of 0.3 e. (b) N−N (solid lines) and B−N (dash lines) bond lengths in the F-BN_5-1 (red line with filled symbols) and F-BN_5-2 (blue line with hole symbols) nanofilms as functions of doped electrons per supercell. Insets illustrate the calculated electron localization function across the N−N bond under different doping levels. (c) Spin-resolved electronic band structures of the F-BN_5-2 nanofilm at (left) neutral, (middle) 0.2 e, and (right) 0.4 e doping level. The states in blue lines with circles are the nearly free electron states, while the lines with squares mark the antibonding state from the N−N bond. The insets in (c) are the charge density distributions of the nearly free electron states under different doping levels, with red and blue colors representing highest and lowest values, respectively.

state, whose partial occupation thus provokes the spin-polarization. To confirm this physical picture, we first examine the bond length variations in both the electron-doped nanofilms. As shown in Figure 6b, the N−N bond's length in both nanofilms sharply elongates upon electron doping, in contrast to other B−N bonds that are only slightly changed. The elongated N−N bonds create localized dangling bond states because partial N electrons now do not participate in forming the chemical bonds. This is reflected in the spin-polarized band structures of the F-BN_5-2 nanofilm under different doping levels (Figure 6c). Indeed, the dispersion of the minimum conduction band (line with triangles) is reduced with increasing doping level and therefore becomes more and more localized. The localized partially occupied band shows a spin splitting once the Stoner criterion[31] is met, and its spin polarization dominates the magnetism of the system. Even so, the minimum conduction band still maintains an appreciable dispersion, which provides extended tails of wave functions for overlapping among each other and accounts for the ferromagnetic coupling between local spins. In Figure 6c, we also notice another conduction band (line with circle) dropping considerably in energy relative to the other bands and cutting the Fermi level at 0.4 e extra electron. This state is a nearly free electron state weakly bound to the nanofilm and retreats aside to the vacuum region due to an electrostatic interaction[32] (see inset in Figure 6c). This behavior of the nearly free electron state has been widely explored in the sp^2-bond system[29] but is seldom addressed in sp^3-bond materials. The redistributed nearly

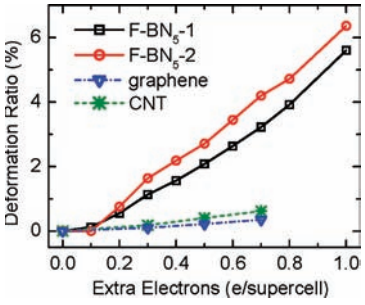

Figure 7. Electron doping induced thickness deformation of the F-BN_5-1 and F-BN_5-2 nanofilms. The doping-induced deformation ratio in carbon nanotubes and graphene exacted from ref 35 is also drawn for comparison.

free electron state will form a 2D electron gas in the doped *c*-BN nanofilms and, together with the spin-polarized channel along the N−N bond layer, carries the electric transport along the nanofilm.

Note that the doping-induced ferromagnetism in the formed namofilms is from a unique mechanism due to the N−N bond layer: carrier-driven stretching of chemical bonds that produces dangling bond states for spin polarization. This is in contrast to the hole-induced ferromagnetism in first-row d_0 semiconductors due to the localized valence electrons of the anions.[33] For our F-BN_m nanofilms, all the doping-induced structural and

dx.doi.org/10.1021/ja206703x |*J. Am. Chem. Soc.* 2011, 133, 14831–14838

magnetic behaviors are absent with hole doping because the VBM is derived from the surface B−F bonds which are inert to carrier doping. Importantly, the doping levels studied above are quite feasible, which can be realized by using either field-effect structures or charge-transfer cationic dopants, such as alkali atoms.[34]

Along with the doping-induced bond elongation, the nanofilms naturally suffer an expansion in thickness. Figure 7 shows the deformation ratio of thickness for the F-BN_5-1 and F-BN_5-2 nanofilms as a function of the doping level, which can reach up to 2.1% and 2.7% at a moderate 0.4 e extra electrons, respectively, mostly contributed by the elongation of N−N bonds. At the same doping level, these deformation ratios are nearly 1 order of magnitude larger than the reported values (∼0.3%) in carbon nanotubes and graphene as shown also in Figure 7.[34,35] Considering the excellent mechanical properties inherited from *c*-BN, such superb electromechanical properties render the proposed BN nanofilms very promising in energy conversion devices, such as actuators.[36]

Further analysis of electron localization function shows that the N−N bond in both the F-BN_5 nanofilms is broken when the extra electron level reaches 0.6 e per supercell (see the inset at 0.6 e in Figure 6b). The bond breaking can be recovered when the electron doping is switched off. These results indicate the BN nanofilms undergo a reversible cleavage along the N−N bond layer and can form two separate single-crystal *c*-BN slabs at high doping levels. Through passivating the N-ended surface of both the BN slabs with hydrogen (low electronegativity), we obtain two thinner single-crystal BN nanofilms with high stability. These newly formed BN nanofilms have robust structure against electron doping and excellent electronic properties as well for applications (see Figure S4 in Supporting Information).

4. CONCLUSIONS

Our systematical first-principles calculations show that surface fluorination of few-layered *h*-BN sheets can lead to formation of thermodynamically favorable F-terminated *c*-BN nanofilms with an embedded N−N bond layer and strong inbuilt electric polarization that controls the band gap of the formed nanofilms. It is found that coupling of externally applied fields to this inbuilt polarization can be used to effectively modulate the band gaps of the nanofilms. Significantly, by electron doping within reasonable levels, the produced nanofilms exhibit substantial ferromagnetism along the N−N bond layer and an exceptionally large deformation that is 1 order of magnitude higher than carbon nanotubes and graphene. At a sufficient high doping level, the nanofilm is cleaved from the N−N bond layer into two thinner BN films. As the proposed synthesis strategy using fluorination is well within the reach of current technologies, our results shed new light on synthesizing the promising *c*-BN nanofilms for applications in nanoelectronics, photovoltaic, and actuators.

■ ASSOCIATED CONTENT

Supporting Information. Total energy and structures of some polymorphs for the *c*-BN_m nanofilm, snapshot of ab initio molecular dynamics simulation, and band structures of the cleaved BN nanofims are collected. This material is available free of charge via the Internet at http://pubs.acs.org.

■ AUTHOR INFORMATION

Corresponding Author
wlguo@nuaa.edu.cn; xczeng@phase2.unl.edu

■ ACKNOWLEDGMENT

ZZ and WG are supported by the 973 Program (2007CB936204), National NSF (11172124, 10732040, 91023026), and Jiangsu Province NSF (BK2008042) of China. XCZ is supported by ARL (W911NF1020099), NSF (DMR-0820521), and ONR (N00014-09-1-0943) and by the University of Nebraska's Holland Computing Center.

■ REFERENCES

(1) Liu, A. Y.; Cohen, M. L. *Science* **1989**, *245*, 841–842.
(2) Teter, D. M.; Hemley, R. J. *Science* **1996**, *271*, 53–55.
(3) El Khakani, M. A.; Chaker, M. *J. Vac. Sci. Technol. B* **1993**, *11*, 2930–2937.
(4) Mirkarimi, P. B.; McCarty, K. F.; Medlin, D. L. *Mater. Sci. Eng. R.* **1997**, *21*, 47–100.
(5) Mishima, O.; Tanaka, J.; Yamaoka, S.; Fukunaga, O. *Science* **1987**, *238*, 181–183.
(6) Mineta, S.; Kohata, M.; Yasunaga, N.; Kikuta, Y. *Thin Solid Films.* **1990**, *189*, 125–138.
(7) Zhang, W.; Bello, I.; Lifshitz, Y.; Chan, K. M.; Meng, X.; Wu, Y.; Chan, C. Y.; Lee, S. T. *Adv. Mater.* **2004**, *16*, 1405–1408.
(8) Zhang, X. W.; Boyen, H.-G.; Deyneka, N.; Ziemann, P.; Banhart, F.; Schreck, M. *Nat. Mater.* **2003**, *2*, 312–315.
(9) Lux, B.; Kalss, W.; Haubner, R.; Taniguchi, T. *Diamond Relat. Mater.* **1999**, *8*, 415–422.
(10) Chong, Y. M.; Ma, K. L.; Leung, K. M.; Chan, C. Y.; Ye, Q.; Bello, I.; Zhang, W.; Lee, S. T. *Chem. Vap. Deposition* **2006**, *12*, 33–38.
(11) Zhang, W. J.; Meng, X. M.; Chan, C. Y.; Chan, K. M.; Wu, Y.; Bello, I.; Lee, S. T. *J. Phys. Chem. B* **2005**, *109*, 16005–16010.
(12) Vel, L.; Demazeau., G.; Etourneau, J. *Mater. Sci. Eng., B* **1991**, *10*, 149–164.
(13) Nair, R. R.; Ren, W.; Jalil, R.; Riaz, I.; Kravets, V. G. *Small* **2010**, *6*, 2877–2884.
(14) Jeon, K. J.; Lee, Z.; Pollak, E.; Moreschini, L.; Bostwick, A.; Park, C. M. *ACS Nano* **2011**, *5*, 1042–1046.
(15) Zhou, J.; Wang, Q.; Sun, Q.; Jena, P. *Phys. Rev. B* **2010**, *81*, 085442.
(16) Zhang, Z. H.; Guo, W. L. *J. Am. Chem. Soc.* **2009**, *131*, 6874–6879.
(17) Xiang, H. J.; Yang, J.; Hou, J. G.; Zhu, Q. *Appl. Phys. Lett.* **2005**, *87*, 243113.
(18) Zhou, Z.; Zhao, J.; Chen, Z.; Schleyer, P. R. *J. Phys. Chem. B* **2006**, *110*, 25678–25685.
(19) Robinson, J. T.; Burgess, J. S.; Junkermeier, C. E.; Badescu, S. C.; Reinecke, T. L.; Perkins, F. K.; Zalalutdniov, M. K.; Baldwin, J. W. *Nano Lett.* **2010**, *10*, 3001–3005.
(20) Hornekær, L.; Rauls, E.; Xu, W.; Sljivancanin, Z.; Otero, R.; Stensgaard, I.; Lægsgaard, E. *Phys. Rev. Lett.* **2006**, *97*, 186102.
(21) Song, L.; Ci, L.; Lu, H.; Sorokin, P. B.; Jin, C.; Ni, J.; Kvashnin, A. G.; Kvashnin, D. G.; Lou, J.; Yakobson, B. I.; Ajayan, P. M. *Nano Lett.* **2010**, *10*, 3209–3215.
(22) Kresse, G.; Hafner, J. *Phys. Rev. B* **1994**, *49*, 14251–14269.
(23) Kresse, G.; Furthmuller, J. *Phys. Rev. B* **1996**, *54*, 11169–11186.
(24) Blochl, P. E. *Phys. Rev. B* **1994**, *50*, 17953–17979.
(25) Neugebauer, J.; Scheffler, M. *Phys. Rev. B* **1992**, *46*, 16067–16080.
(26) Fahy, S.; Wang, X. W.; Louie, S. G. *Phys. Rev. B* **1990**, *42*, 3503–3522.
(27) The energy barrier is calculated using the climbing image nudged elastic band method. Mills, G.; Josson, H.; Schenter, G. K. *Surf. Sci.* **1995**, *324*, 305–337. Henkelman, G.; Uberuaga, B. P.; Jónsson, H. *J. Chem. Phys.* **2000**, *113*, 9901–9904.

(28) Gratzel, M. *Nature* **2001**, *414*, 338–344.
(29) Zhang, Z.; Guo, W. *Phys. Rev. B* **2008**, *77*, 075403.
(30) Khoo, K. H.; Mazzoni, M. S. C.; Louie, S. G. *Phys. Rev. B* **2004**, *69*, 201401R.
(31) Edwards, D. M.; Katsnelson, M. I. *J. Phys.: Condens. Matter* **2006**, *18*, 7209–7225.
(32) Margine, E. R.; Crespi, V. H. *Phys. Rev. Lett.* **2006**, *96*, 196803.
(33) Peng, H.; Xiang, H. J.; Wei, S. H.; Li, S.; Xia, J.; Li, J. *Phys. Rev. Lett.* **2009**, *102*, 017201.
(34) Sun, G.; Kurti, J.; Kertesz, M.; Baughman, R. H. *J. Am. Chem. Soc.* **2002**, *124*, 15076–15080.
(35) Verissimo-Alves, M.; Koiller, B.; Chacham, H.; Capaz1, R. B. *Phys. Rev. B* **2003**, *67*, 161401R.
(36) Baughman, R. H.; Cui, C.; Zakhidov, A. A.; Iqbal, Z.; Barisci, J. N. *Science* **1999**, *284*, 1340.